AGU PUBLICATIONS

JGR

Journal of Geophysical Research: Oceans

RESEARCH ARTICLE

10.1002/2015JC011211

The distribution of glacial meltwater in the Amundsen Sea, Antarctica, revealed by dissolved helium and neon

Intae Kim[1], Doshik Hahm[1,2], Tae Siek Rhee[1], Tae Wan Kim[1], Chang-Sin Kim[1], and SangHoon Lee[1]

[1]Division of Polar Ocean Environment, Korea Polar Research Institute, Incheon, South Korea, [2]Now at Department of Oceanography, Pusan National University, Busan, South Korea

Key Points:
- Large excess of He and Ne, attributable to glacial melting, were observed in the Amundsen Sea
- Glacial meltwater is transported over 300 km offshore in the Amundsen Sea
- Strong temporal variation of glacial meltwater was observed between 2011 and 2012

Supporting Information:
- Supporting Information S1

Correspondence to:
D. Hahm,
hahm@pusan.ac.kr

Citation:
Kim, I., D. Hahm, T. S. Rhee, T. W. Kim, C.-S. Kim, and S.H. Lee (2016), The distribution of glacial meltwater in the Amundsen Sea, Antarctica, revealed by dissolved helium and neon, *J. Geophys. Res. Oceans*, *121*, 1654–1666, doi:10.1002/2015JC011211.

Received 7 AUG 2015
Accepted 1 FEB 2016
Accepted article online 6 FEB 2016
Published online 12 MAR 2016

Abstract The light noble gases, helium (He) and neon (Ne), dissolved in seawater, can be useful tracers of freshwater input from glacial melting because the dissolution of air bubbles trapped in glacial ice results in an approximately tenfold supersaturation. Using He and Ne measurements, we determined, for the first time, the distribution of glacial meltwater (GMW) within the water columns of the Dotson Trough (DT) and in front of the Dotson and Getz Ice Shelves (DIS and GIS, respectively) in the western Amundsen Sea, Antarctica, in the austral summers of 2011 and 2012. The measured saturation anomalies of He and Ne (ΔHe and ΔNe) were in the range of 3–35% and 2–12%, respectively, indicating a significant presence of GMW. Throughout the DT, the highest values of ΔHe (21%) were observed at depths of 400–500 m, corresponding to the layer between the incoming warm Circumpolar Deep Water and the overlying Winter Water. The high ΔHe (and ΔNe) area extended outside of the shelf break, suggesting that GMW is transported more than 300 km offshore. The ΔHe was substantially higher in front of the DIS than the GIS, and the highest ΔHe (31%) was observed in the western part of the DIS, where concentrated outflow from the shelf to the offshore was observed. In 2012, the calculated GMW fraction in seawater based on excess He and Ne decreased by 30–40% compared with that in 2011 in both ice shelves, indicating strong temporal variability in glacial melting.

1. Introduction

Basal melting of marine ice shelves, which is occurring at a rate of 1300–1500 Gt yr^{-1}, is, along with ice calving, the process most responsible for the mass loss of the Antarctic ice sheet [*Pritchard et al*., 2012; *Depoorter et al*., 2013; *Rignot et al*., 2013]. It is also known that the majority of basal melting occurs in West Antarctica, where the warm Circumpolar Deep Water (CDW) intrudes through deep troughs and reaches the grounding line of the ice shelves [*Jacobs et al*., 2011; *Depoorter et al*., 2013]. Basal melting also affects water circulation by introducing glacial meltwater (GMW) into the ocean. For example, buoyancy forcing by exported GMW influences the formation of the cyclonic gyre in Pine Island Bay [*Thurnherr et al*., 2014]. Long-term observations [*Jacobs et al*., 2002; *Jacobs and Giulivi*, 2010] and a recent modeling study [*Nakayama et al*., 2014] suggest that the increased meltwater around western Antarctica is responsible for the freshening of the Ross Sea, which may result in a change in the Antarctic Bottom Water formation.

The Pine Island Glacier ice shelf (PIIS) in the eastern Amundsen Sea has long been a place to observe the rapid melting of the ice shelf and its interaction with the CDW. *Jacobs et al*. [2011] showed that the temperature and volume of deep water in Pine Island Bay (PIB) increased in 2009 compared to those in 1994, indicating that the rise of meltwater production of the PIIS results from stronger deep water circulation under the ice shelf. *Dutrieux et al*. [2014] extended those observations to 2012 and argued that melting decreased by 53% between 2010 and 2012 and that the reduced melting is partly attributable to strong easterly wind anomalies in the Amundsen Sea possibly associated with a La Niña event.

Compared with PIB and the PIIS in the eastern Amundsen Sea, the Dotson Trough (DT) and the adjacent Dotson and Getz ice shelves (DIS and GIS, respectively) in the western Amundsen Sea have received limited attention with respect to glacial melting (Figure 1). The current understanding of the GMW distribution around the DT is based on only a few studies. *Wåhlin et al*. [2010] first reported that meltwater occupied a 100–150 m thick layer (at a depth of 400–550 m) between the incoming modified CDW (mCDW; defined as $\theta > 1.5$°C and S $\approx$ 34.7) and Winter Water (WW; defined as $\theta \approx -1.7$°C, S $\approx$ 34.0) during their 2008 expedition, based on hydrographic observations (supporting information Figure S1). *Randall-Goodwin et al*. [2015]

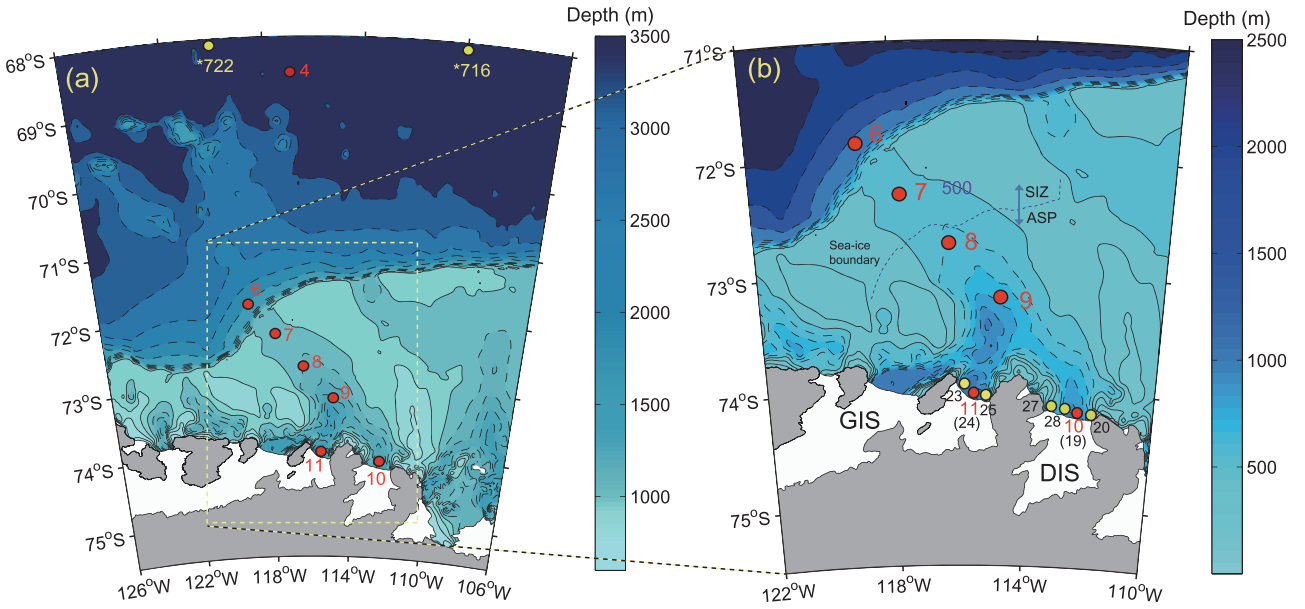

Figure 1. (a) Map of the study area. The red circles represent the sampling stations in 2011, and the yellow circles indicate Sts. 722 and 716 of the WOCE S4P line, where He and Ne data have previously been reported [*Hohmann et al.*, 2002]. (b) Enlarged view of the sampling stations in the DT. The red and yellow circles represent the stations in 2011 and 2012, respectively. Stations 10 (DIS) and 11 (GIS) overlapped stations 19 (DIS) and 24 (GIS), respectively, on the 2012 cruise. The dotted line between stations 7 and 8 indicates the sea-ice boundary between the Amundsen Sea Polynya (ASP) and the sea-ice zone (sea-ice concentration > 10%).

showed that a melt-laden outflow emanated from the DIS and flowed between 400 and 600 m throughout the DT, based on hydrographic observations in the austral summer of 2010/2011. *Randall-Goodwin et al.* [2015] also observed that the outflow from the DIS was concentrated on the western side of the DIS. In this region, *Ha et al.* [2014] estimated a glacial melting rate of 83–316 Gt yr^{-1}, with an intermediate value of 237 Gt yr^{-1}, based on an ocean-to-glacier heat flux of 0.9–2.53 TW.

In this study, we sought to address the following questions. (1) How is GMW distributed within the water columns of the DT and DIS? (2) How different are the GMW distributions along the DIS and GIS? (3) Is there significant temporal variation in the GMW distributions? Unlike most previous studies, which mainly relied on measurements of temperature, salinity, and oxygen to quantify the meltwater fraction, we used the concentrations of light noble gases, i.e., helium (He) and neon (Ne) [*Schlosser*, 1986; *Hohmann et al.*, 2002; *Loose and Jenkins*, 2014]. This approach was based on the fact that a complete dissolution of air bubbles trapped in glacial ice results in the supersaturation of He and Ne in the meltwater by approximately 1060% and 770%, respectively [*Weiss*, 1971; *Hohmann et al.*, 2002]. Herein, we report that (1) GMW persists throughout the DT and even beyond the continental shelf, >300 km from the DIS; (2) the GMW distributions along the GIS and DIS show a stark contrast despite their locational proximity (~50 km distance); and (3) there was a substantial reduction in the GMW near the ice shelves between 2011 and 2012.

2. Materials and Methods

2.1. Sampling and Analytical Procedures

The observations and sampling were conducted during the Amundsen Sea cruises of January 2011 and February 2012 onboard RV Araon. To investigate the GMW distribution, we collected vertical profiles of CTD (SBE 911plus with a SBE43 dissolved oxygen sensor) and water samples for noble gas analysis along the DT, from the continental shelf break to an area near the ice shelves (DIS and GIS). The ice shelf stations (Sts. 10 and 11 in 2011; Sts. 19, 20, 27, and 28 of the DIS and 23, 24, and 25 of the GIS in 2012) were no farther than 1 km from the corresponding ice shelves (Figure 1). The dissolved oxygen (DO) from the CTD sensor was compared with bottle values determined by the spectrophotometric Winkler method [*Labasque et al.*, 2004]. The differences between the sensor and bottle measurements were <2%. Because the differences were very close to the accuracy of bottle measurements of ~1%, we did not apply any correction to the values of the DO sensor.

Water samples for noble gas analysis were collected in fresh copper tubes using the cold crimping method described by *Young and Lupton* [1983]. The dissolved gases in the copper tubes were vacuum extracted from the water samples into glass ampoules with low He permeability [*Jenkins et al.*, 1991]. The extracted gases in the ampoules were further cleaned using getters and cryogenic cold traps and then measured in a mass spectrometer as described by *Stanley et al.* [2009]. The gas extraction and measurements were conducted at the Isotope Geochemistry Facility, Woods Hole Oceanographic Institution. Measurements were made to an accuracy of approximately 1.0% and precisions of less than 0.5% for He and Ne. The results were corrected for processing blanks and extraction efficiencies by an amount generally less than the measurement precision.

2.2. Notation for Noble Gases

In this study, the δ notation is used to present the isotopic $^3He/^4He$ ratio relative to the atmospheric $^3He/^4He$ ratio ($R_a = 1.384 \times 10^{-6}$) [*Clarke et al.*, 1976] according to the following equation:

$$\delta^3He = \{(^3He/^4He)/R_a - 1\} \times 100\% \quad (1)$$

The saturation anomalies of He and Ne were calculated by the following equations:

$$\Delta He = (He/He_{eq} - 1) \times 100\% \quad (2)$$

$$\Delta Ne = (Ne/Ne_{eq} - 1) \times 100\% \quad (3)$$

where He_{eq} and Ne_{eq} are the concentrations of He and Ne at equilibrium with the atmosphere, respectively [*Weiss*, 1971].

2.3. Processing of Current Data

Vertical current profile data were obtained using a 300 kHz Lowered Acoustic Doppler Current Profiler (LADCP) from Teledyne RD Instruments. The processing of the LADCP data was performed according to *Thurnherr* [2010]. The velocity profiles were detided using 10 major components of a barotropic tide model [*Padman et al.*, 2002].

3. Results and Discussion

3.1. Observations Along the Dotson Trough in 2011

The vertical distributions of salinity (S), potential temperature (θ), and DO are shown in Figure 2 (Figure S1). At St. 4, located 400 km from the continental shelf break of the Amundsen Sea, the subsurface layer deeper than 300 m depth was occupied by CDW (defined as $\theta > 1.5$°C, S ≈ 34.7 and DO ≈ 170–187 μmol kg^{-1} in this study) [*Wåhlin et al.*, 2010]. Near the continental shelf (St. 6), the waters at the middepth layer between 300 and 500 m were much fresher and colder than at St. 4, likely due to the gradual modification of CDW by mixing with WW (defined as $\theta \approx -1.7$°C, S ≈ 34.0 and DO ≈ 260–270 μmol kg^{-1} in this study) [*Wåhlin et al.*, 2010]. WW was more evident at stations on the continental shelf (Sts. 7–11), occupying the water layer shallower than 400 m (supporting information Figure S1). The surface layer water (<200 m) on top of the WW layer was fresher and warmer than the WW, due to sea-ice melting and surface heating by solar radiation. The waters below the WW layer became saltier and warmer than the WW with increasing depth, indicating a mixing of the WW with modified CDW (mCDW, defined as $\theta \approx 1.0$°C and S ≈ 34.5 in this study) [*Wåhlin et al.*, 2010] (supporting information Figure S1). At Sts. 10 and 11, located <1 km from the DIS and GIS, respectively, mCDW occupied more than 200 m of the bottom layer. We note that the middepth layer (400–600 m) at St. 10 exhibited higher θ and S and lower DO ($\theta \approx -1$ to 0°C, S ≈ 34.2–34.4 and DO ≈ 200–250 μmol kg^{-1}) than the other stations. This agrees with the fact that the main pathway of the CDW is closer to the eastern side of DT [*Ha et al.*, 2014], resulting in warmer, saltier, and less oxygenated water at St. 10 (DIS) relative to St. 11 (GIS) at those depths. In addition, at the shallower depths (200–400 m), higher θ and lower DO indicate a more pronounced local mixing between the mCDW and overlying WW at the DIS than the GIS.

The vertical distribution of the He isotopic ratio, δ^3He, of the DT in 2011 is shown in Figure 3. Generally, δ^3He values at surface ocean are close to the equilibrium value of −1.8% [*Benson and Krause*, 1980] as a result of air-sea gas exchange. Elevated δ^3He values in subsurface layers are due to the decay of tritium

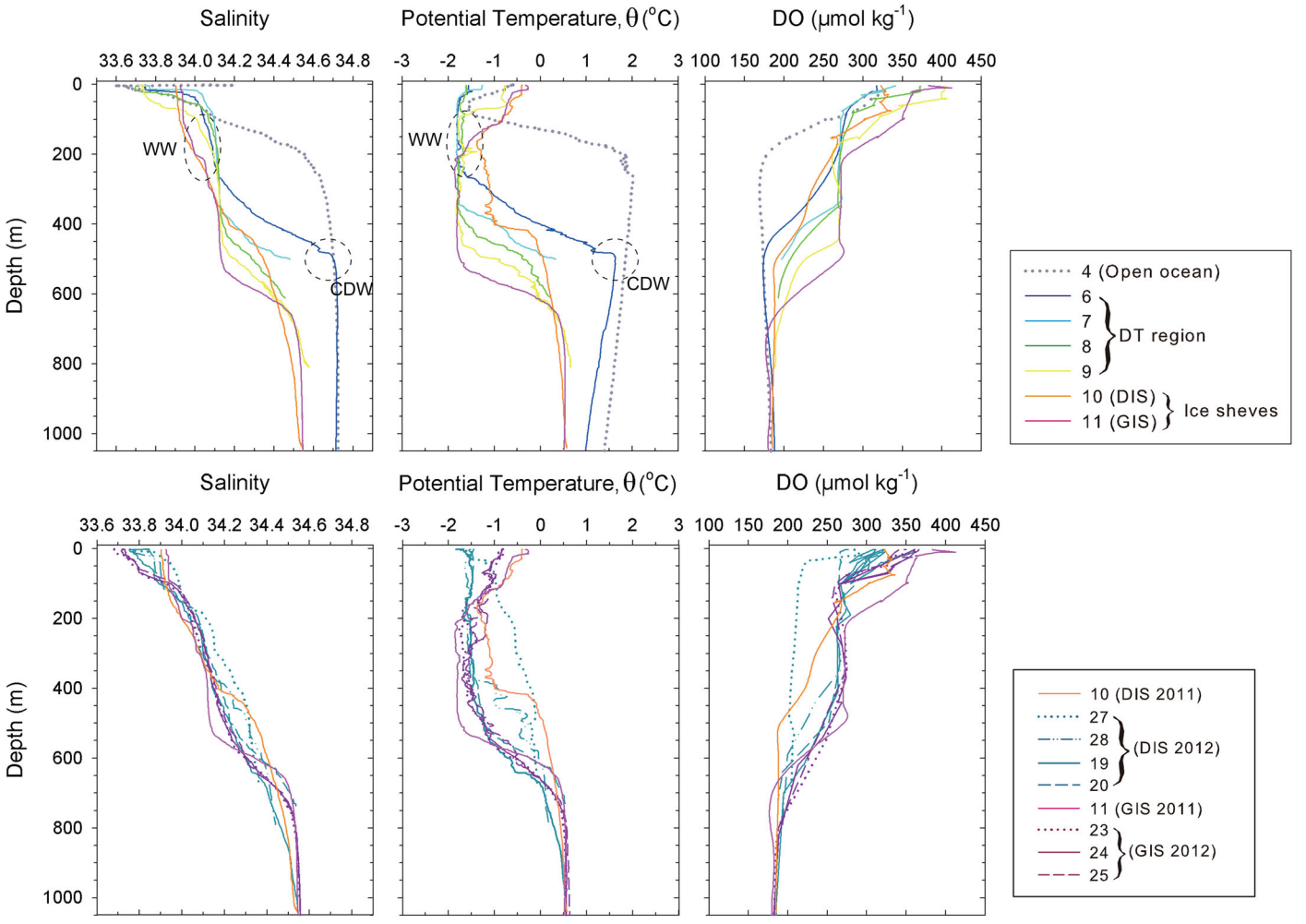

Figure 2. Hydrographic data (top) along the DT in 2011 and (bottom) along the ice shelves (DIS and GIS) in 2012. For an interannual comparison, data from the DIS (St. 10) and GIS (St. 11) in 2011 were included in the 2012 data sets (bottom plots).

(^{3}H) or/and addition of mantle He from submarine hydrothermal systems, which is about tenfold enriched in ^{3}He relative to atmospheric He. Considering the low ^{3}H concentrations in the Southern Ocean, the elevated values in subsurface layers of the South Pacific are ascribed to the mantle He [*Hohmann et al*., 2002; *Winckler et al*., 2010]. The conservative behavior of He makes δ^3He a useful tracer for water mass identification. The vertical profile of δ^3He in the DT (Sts. 6–11) showed a gradual increase with depth and remained nearly constant at the bottom, with δ^3He values of ~9%. These high δ^3He values in the DT were similar or slightly less than those in the deep water of St. 4 (up to 10%). The slightly less δ^3He in the DT than at St. 4 is likely due to the gradual modification of the CDW by mixing with WW, consistent with the freshening and cooling shown in θ and S profiles (Figure 2). Near the surface, the water appeared to lose excess ^{3}He through gas exchange, reaching values close to the static equilibrium value of −1.8% [*Benson and Krause*, 1980]. The δ^3He values at the DIS (St. 10) were much higher (3–9%) at middepth (200–600 m) than at the GIS (St. 11) or the DT (Sts. 6–9). This is probably due to a combined effect of shallower thermocline [*Ha et al*., 2014] and enhanced vertical mixing between the mCDW and WW at the DIS, which is also consistent with the higher θ and S and lower DO values at St. 10.

The vertical distributions of the ΔHe and ΔNe of the DT in 2011 are shown in Figure 3. Both the ΔHe and ΔNe in the layer between 300 and 1000 m at St. 4 were within the narrow ranges of 6–7% and 3–4%, respectively. These values are consistent with values previously reported by *Hohmann et al*. [2002] at WOCE line S4P (5–6% and 3–4%, respectively; refer to *Hohmann et al*. [2002, Figures 9a and 9b]). Compared with the open ocean values at St. 4, the ΔHe and ΔNe values were much higher at all of the stations on the

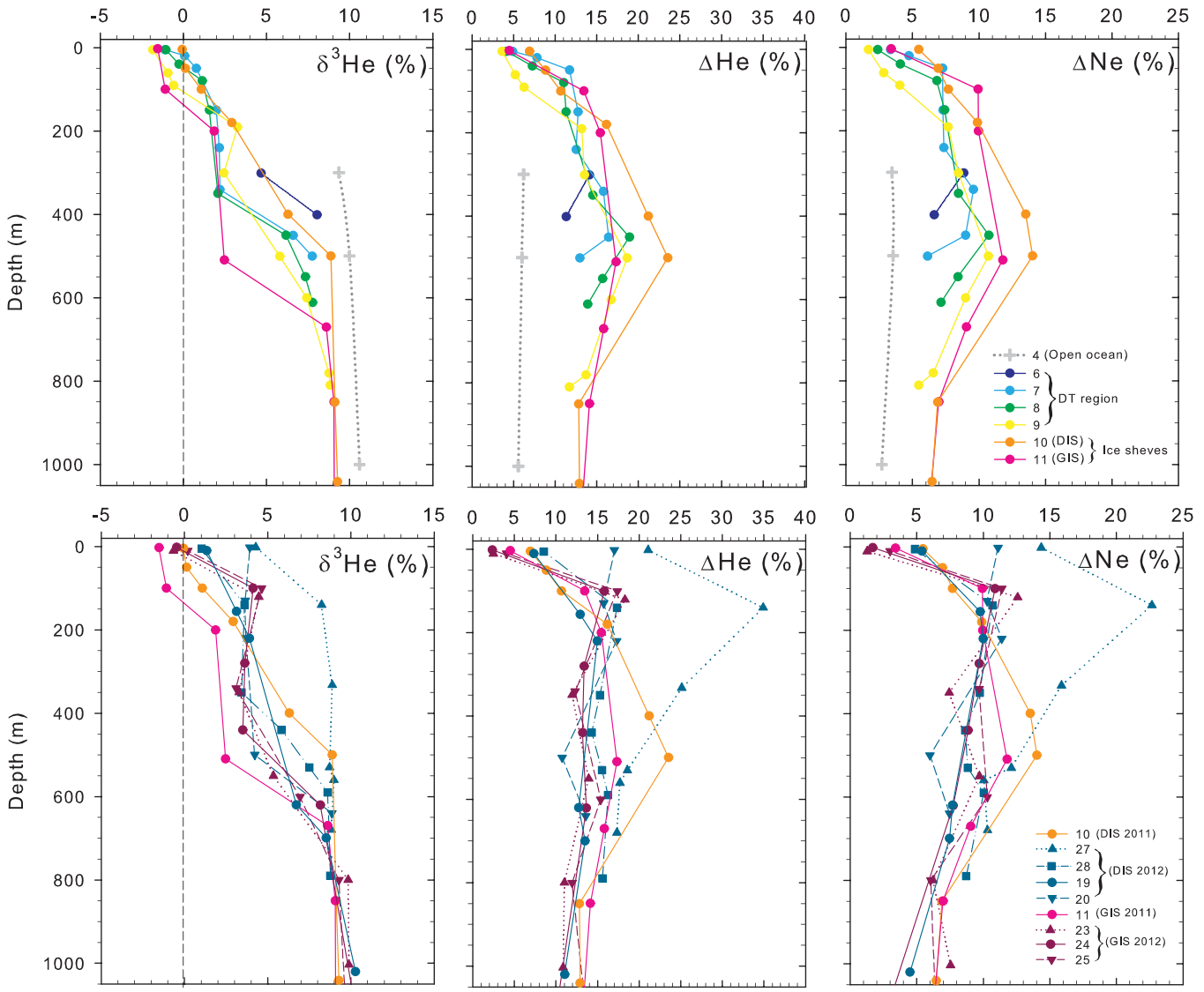

Figure 3. The measured (top) δ^3He, ΔHe, and ΔNe data in 2011 and (bottom) the ice shelves (DIS and GIS) in 2012. Data in 2011 at the DIS (St. 10) and GIS (St. 11) were compared with those in 2012 (bottom plots) for an interannual comparison.

continental shelf. Ignoring the surface layer, which is subject to gas exchange with the atmosphere, the ΔHe at depths greater than 200 m were in the range of 12–24%, suggesting that there are processes responsible for the additional ΔHe of 5–17% in the Amundsen Sea. The excess is most likely due to GMW input. The origin of these excess ΔHe and ΔNe was discussed in section 3.3. The maximum ΔHe (and ΔNe) was observed at a depth of ~500 m at each station, and the ΔHe increase at this depth became more distinct closer to the DIS.

3.2. Observations Along the Dotson and Getz Ice Shelves in 2012

In 2012, we conducted CTD casts along the DIS and GIS (<1 km from the ice shelves) to investigate the spatial variation of the water properties in front of the ice shelves (Figure 1). The stations near the GIS (Sts. 23–25 from the west to east) all exhibited nearly identical vertical profiles of S, θ, and DO (Figure 2), indicating no evident spatial variation in water properties along the GIS. However, substantial variations were observed along the DIS. For example, the vertical profiles of S and θ at middepth at the stations in the westernmost part of the DIS (St. 27) were significantly higher than those at the other stations, whereas the vertical profiles at the other stations of the DIS largely overlapped with those at the GIS. Similarly, DO at St. 27 was significantly lower (up to 280 μmol kg^{-1}) than at the other DIS stations (up to 330 μmol kg^{-1}). All of

these deviations of S, θ, and DO along the DIS indicate that most of the seaward outflow, a mixture of mCDW (with high S and θ and low DO) with GMW, spread out from the western part of the DIS. This is consistent with the findings of inflows on the eastern sides and outflows on the western sides of the ice shelf openings in many Getz ice shelves [*Jacobs et al*., 2013]. We note that the GIS in this study is the easternmost ice shelf among many ice shelves collectively called the "Getz Ice Shelf" in *Jacobs et al*. [2013] and that the GIS showed the least along-shelf variation in outflow of these ice shelves, consistent with our results.

We also note that the water properties determined at the center of the DIS displayed marked differences between 2011 and 2012. Although St. 19 in 2012 was <700 m apart from St. 10 in 2011, the substantially elevated S and θ at middepth in 2011 was not observed in 2012. By contrast, θ at middepth (200–600 m) decreased by almost 1°C. This discrepancy between 2011 and 2012 at the DIS was not evident at the GIS (Figure 2).

The overall vertical distributions of δ^3He were similar to those in 2011, showing a gradual increase with increasing depth. However, there were some differences between each ice shelf. At the DIS, higher δ^3He values were observed at depths of 100–600 m for St. 27 (8–9% versus 4–6%) and the surface water of Sts. 20 and 27 (∼4% versus −2 to 1%) at corresponding depths of the other profiles. These high δ^3He values indicate that a substantial amount of deep water with high δ^3He had upwelled to the surface layer. Interestingly, the high surface value at St. 20 was almost identical to the subsurface values. This suggests that the water had remained under the ice shelf until recently and had been largely isolated from the atmosphere; otherwise, air-sea gas exchange should bring the high value (∼4% at the surface of St. 20) down close to the equilibrium value of −1.8%, as observed at many of the stations. This further indicates that, although much of the return flow was concentrated in the western side of the DIS [*Randall-Goodwin et al*., 2015], a detectable amount of return flow occasionally emanates from other parts along the ice shelves. At the GIS, the δ^3He values were relatively constant at 100–500 m depth, indicating that the influence of deep water with high δ^3He on this layer is relatively small and spatially homogeneous along the ice shelf.

The ΔHe (and ΔNe) at the DIS and GIS was in the range of 12–18% and 8–12%, respectively, and largely overlapped each other at depths deeper than 100 m, indicating no clear spatial variation along the ice shelves (Figure 3). By contrast, the profile of St. 27, on the western edge of the DIS, exhibited exceptionally high values of ΔHe and ΔNe (up to 35% and 23%, respectively) at depths shallower than 600 m. This trend was also observed in the δ^3He results at this station. Collectively, St. 27 stands out from the other "along-shelf" stations because of its higher S, θ, δ^3He, ΔHe, and ΔNe, and lower DO at middepths.

Notably, both the ΔHe and ΔNe values at St. 19 were significantly lower than those at St. 10 in 2011, although the two stations were <700 m apart. The pronounced maximum ΔHe (23%) at 500 m in 2011 did not exist in 2012. Instead, the ΔHe at 500 m decreased to 15% in 2012. This ∼40% reduction of the ΔHe in 2012 was also found in ΔNe. By contrast, the ΔHe (and ΔNe) difference at the GIS was not as clear as that at the DIS. The 3% difference in the ΔHe, from 17% at St. 11 in 2011 to 14% at St. 24 in 2012, was slightly above the measurement precision <0.5% (Figure 3 and supporting information Figure S2).

3.3. Origin of Excess He and Ne

To identify the origin of the excess He and Ne in the Amundsen Sea, we examined the isotopic ratios of He (^{3}He/^{4}He) and the relationship between the ΔHe and ΔNe. The plot of ^{3}He versus ^{4}He shown in Figure 4a exhibits two separate trends. The first trend (dashed magenta line) starts from the values obtained from St. 4 and follows the mixing line with the atmosphere (^{3}He/^{4}He = 1.384×10^{-6}) [*Clarke et al*., 1976] until finally reaching the maximum He value. Most of the samples from the deep layer (>500 m) fall on this mixing line, and their excesses can be explained by different degrees of addition of the atmospheric component. By contrast, the second trend, formed by the samples from shallower depths (<500 m), exhibits less ^{3}He for the corresponding ^{4}He of the samples from the deep layer. These "shallow" samples fall on the mixing line between air-equilibrated seawater (AEW) and the highest values of He. The AEW values were calculated from the solubility [*Weiss*, 1971] for the mean surface temperature and salinity (in our study area) of −1.14°C and 33.27, respectively, with the assumption of a static equilibrium value of δ^3He (−1.8%) [*Benson and Krause*, 1980] (Figure 4a).

The mCDW has elevated ^{3}He/^{4}He, likely due to the significant presence of mantle He [*Hohmann et al*., 2002; *Winckler et al*., 2010]. Overall, the trends suggest that the mCDW acquires a substantial amount of atmospheric

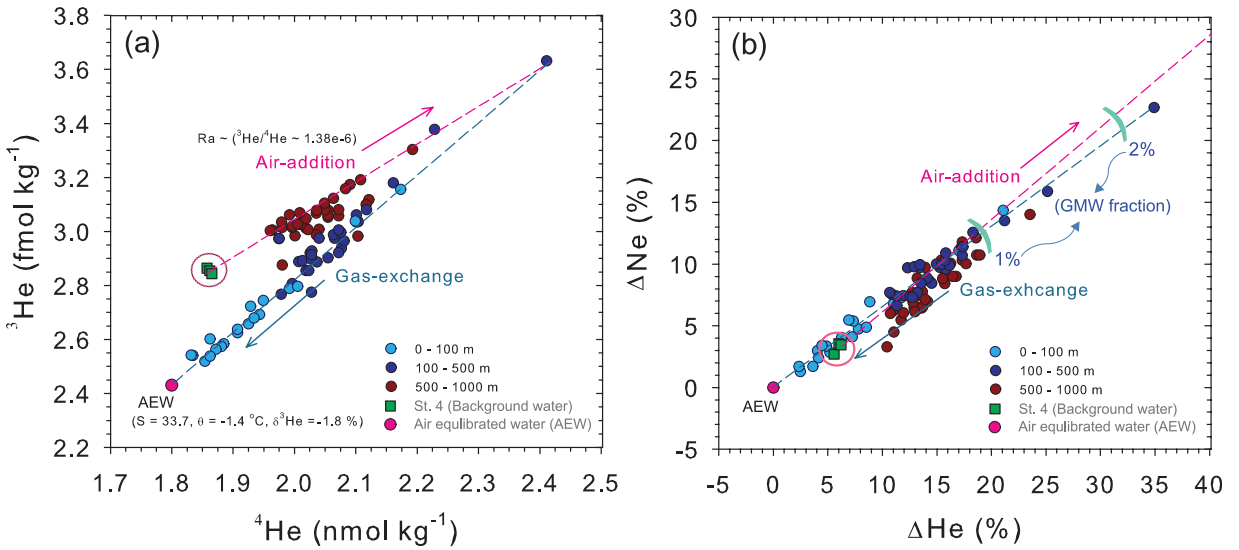

Figure 4. Plots of (a) ^{3}He versus ^{4}He and (b) ΔNe versus ΔHe for the entire data sets from the DT (in 2011) and ice shelves (in 2011 and 2012). Both indicate the predominance of He (and Ne) from the air-addition associated with the GMW input.

He as it approaches the coast of the Amundsen Sea and some of the excesses are lost through air-sea gas exchange at the surface (Figure 4). Deep convection (down to 400–600 m) in winter, responsible for the formation of the WW in the coastal Southern Ocean, appears to be a very effective mechanism promoting the ventilation of the deep layer, which is why some samples at depth fell between the two mixing lines.

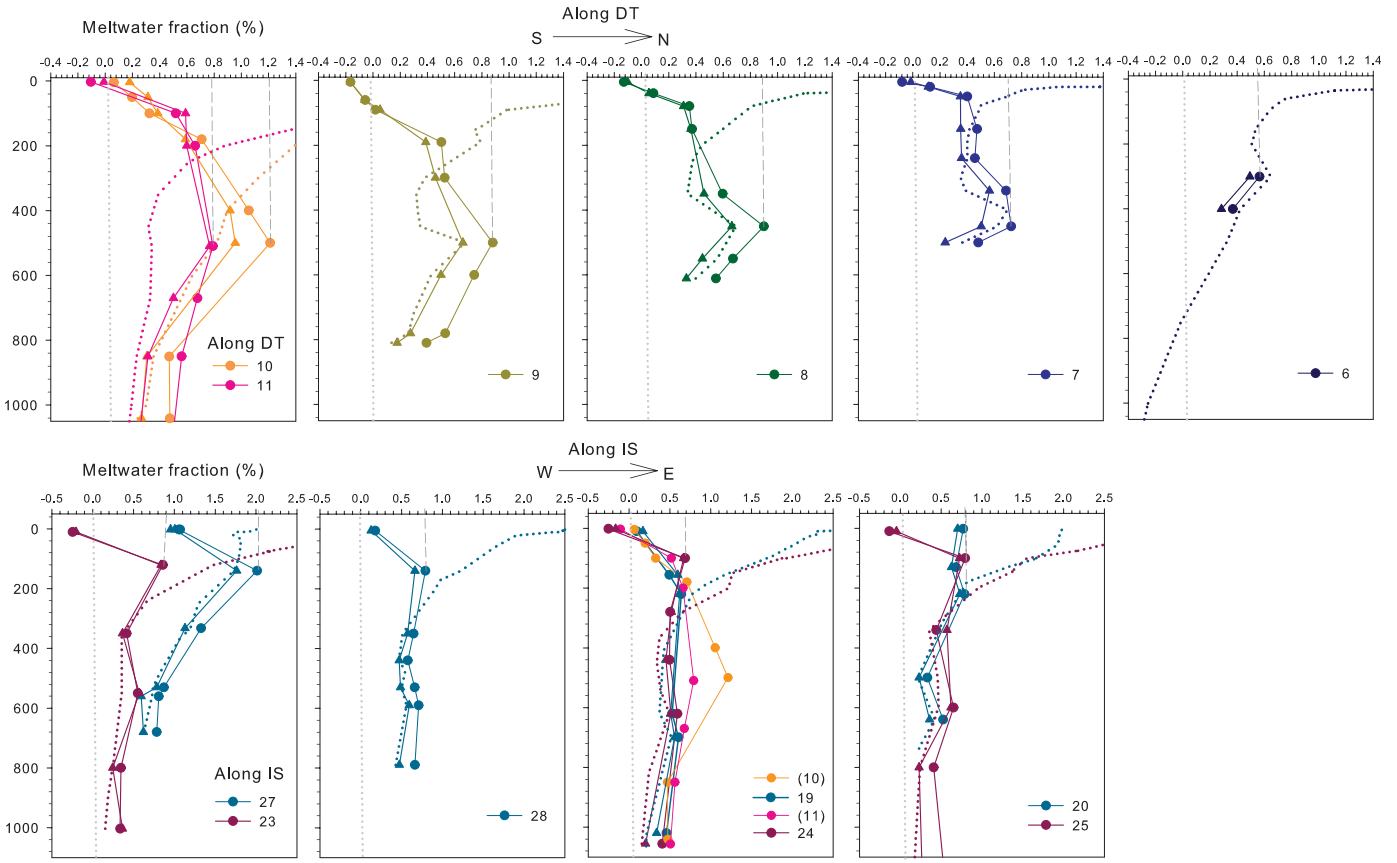

Figure 5. The calculated (top) GMW fraction (%) of the DT (in order from coast to offshore) in 2011 and (bottom) the ice shelves (DIS and GIS) (in order from west to east) in 2012 based on He (circles), Ne (triangles), and the θ-S pairs (dotted lines).

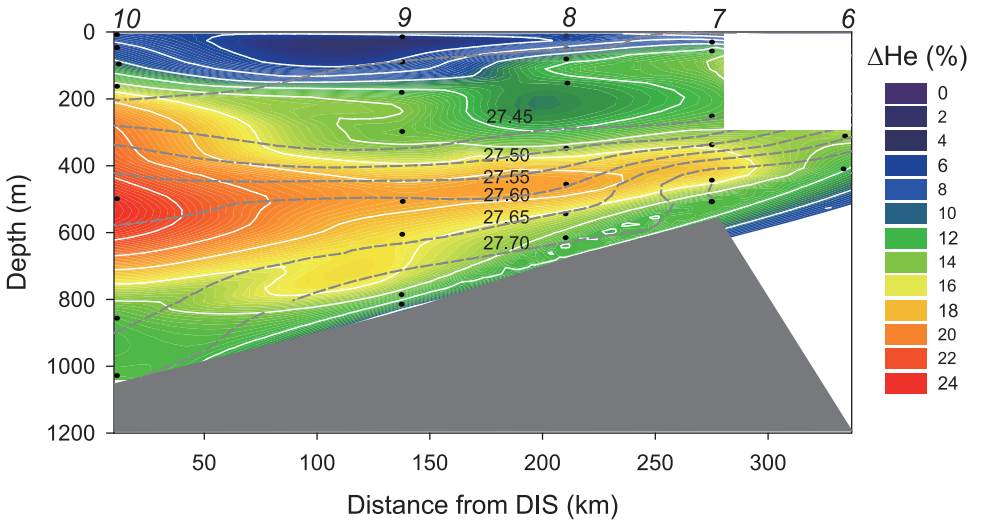

Figure 6. Distributions of ΔHe within the water column of the DT (Sts. 6–10) in 2011. The black dots indicate the sampling depth, and the grey dotted lines indicate the isopycnal lines of σ_θ of 27.4–27.7. The shelf break is located near St. 7 (~280 km from the DIS, St. 10).

The plot of ΔNe versus ΔHe can also be explained by the two aforementioned processes (Figure 4b): (1) the addition of the atmospheric component to St. 4 and (2) the ventilation of the excesses through gas exchange. Because GMW has been identified as the only source that can produce such a large "atmospheric" excess of He and Ne in the polar ocean [e.g., *Schlosser*, 1986; *Hohmann et al*., 2002; *Hahm et al*., 2004], we estimated the ΔHe and ΔNe in seawater mixed with an arbitrary amount of GMW based on the binary mixing of two components, seawater and glacial ice [*Loose and Jenkins*, 2014]. For example, if we assume that 1% of glacial ice (with $S = 0$ and $\theta \approx -90.45$°C) is added to St. 4 (6.0% and 3.5% of ΔHe and ΔNe, respectively) seawater, the ΔHe and ΔNe in the mixed water are mathematically calculated to be 18.7% and 11.7%, respectively. A θ of −90.45°C was determined by extrapolating the θ-S relation to zero salinity based on the observations of *Gade* [1979] and *Jenkins* [1999], who noted that subsurface melt under ice shelves produced a linear relationship for dθ/dS. The observed ΔHe and ΔNe values were consistent with the predicted GMW addition line (Figure 4b), indicating that the large excess ΔHe and ΔNe mainly originated from the GMW addition.

In their Figure 6, *Hahm et al*. [2004] discussed several processes that could alter the ΔHe and ΔNe values. Among them, the sea-ice melting is the only mechanism that can significantly fractionate the Ne/He ratios in our study region. The addition of sea-ice meltwater may result in a depletion of Ne with the addition of He due to the sea-ice/seawater partition coefficients for He (1.12) and Ne (0.66) [*Postlethwaite*, 2002]. For example, the addition of approximately 2.5% of sea-ice meltwater to samples from St. 4 would result in an increase of the ΔHe by 0.6% and a decrease of the ΔNe by 1%, which would be very difficult to discern given the measurement precision of <1%. In the following discussion, we assume that the effects of sea ice on the ratios of the ΔHe and ΔNe are insignificant for our study area.

3.4. Calculation of the GMW Fraction in Seawater Based on Excess He and Ne

We sought to calculate the GMW fraction based on the observed excess He and Ne. The calculation methods were introduced by *Hohmann et al*. [2002]. Briefly, excess He and Ne concentrations from the GMW (He_{GMW} and Ne_{GMW}) are obtained by subtracting the average baseline values (ΔHe_{bl} and ΔNe_{bl}) of the background seawater (with no effect of the GMW) from the measured ΔHe and ΔNe and subsequent unit conversion to absolute concentrations (i.e., Δ% to nmol kg^{-1}). The fraction of GMW (F) is obtained based on He_{GMW} and Ne_{GMW} by the following equation:

$$F = (C_{GMW}/C_{ice}) \times 100\% \quad (4)$$

where C_{GMW} is the excess He and Ne concentrations in the GMW, and C_{ice} is the He and Ne concentrations of the pure GMW.

We determined ΔHe_{bl} and ΔNe_{bl} to be 6.0% and 3.5%, respectively, by averaging the middepth (200–1000 m) values of St. 4 (relative standard deviation = 4.1% and 10.0% for ΔHe and ΔNe, respectively). Our ΔHe_{bl} and ΔNe_{bl} values were also very similar to those of *Hohmann et al*. [2002] observed at WOCE line S4P (in the range 5–6% and 3–4%, respectively). To determine the He and Ne concentrations of pure GMW (C_{ice}), we used the average air content of 0.11 cm^3 STP g^{-1} of the Byrd ice core [*Martinerie et al*., 1992], according to *Hohmann et al*. [2002], and atmospheric He and Ne concentrations of 5.24 and 18.18 ppmv, respectively [*Ozima and Podosek*, 1983]. The calculated values are $[He_{ice}] = 5.76 \times 10^{-7}$ cm^3 STP g^{-1} and $[Ne_{ice}] = 20.0 \times 10^{-7}$ cm^3 STP g^{-1}, which are equivalent to 25.7 and 89.3 nmol kg^{-1} of He and Ne, respectively.

The GMW fractions at each station are shown in Figure 5. The fractions (based on excess He) of the DT, DIS, and GIS seawater at depths >200 m were 0.3–0.8%, 0.3–2.0%, and 0.4–0.8%, respectively (Figure 5). The GMW proportions based on the excess Ne were 0.2–0.7%, 0.2– 1.8%, and 0.2–0.8% in the DT, DIS, and GIS stations, respectively. The GMW fraction based on He was <20% larger than the Ne-based results. *Hohmann et al*. [2002, 2003] have suggested that this difference may result from additional terrigenic He source inputs.

We note that the observed excess He and Ne in the Amundsen Sea could represent the lower limits of the GMW because gas loss at the surface via gas exchange to the atmosphere is not considered in this calculation. *Hohmann et al*. [2002] have suggested that this unrevealed proportion of GMW based on excess He and Ne could be up to 15% in the water column, assuming that the subsurface maximum concentration at several hundred meters should be extended to the surface if there was no gas loss via gas exchange. If we apply this same assumption to our vertical profiles (dotted lines in Figure 5), the GMW fraction would increase by 23–34% for the ice shelves and 36–47% for the DT region, suggesting up to a 47% loss via gas exchange at the surface.

Jenkins [1999] introduced an approach for calculating the meltwater fraction in seawater based on the coupling of two independent variables (e.g., θ, S, and DO concentrations) with the assumption of a three-component mixing of meltwater, WW, and CDW. These calculations have been widely applied in recent ice meltwater studies [*Jenkins and Jacobs*, 2008; *Jacobs et al*., 2011; *Randall-Goodwin et al*., 2015]. We compared our GMW fractions with those from θ-S pairs using the approach of Jenkins [1999] (Figure 5). The θ and S values for the end-members (0.75°C and 34.62 for (m)CDW, −1.84°C and 34.18 for WW, and −90.45°C and 0 for meltwater) were determined based on the observations in 2011 and 2012. Ignoring the shallow layers (0–300 m) where the values are poorly constrained by both approaches, meltwater fractions from both approaches were in a good agreement given the presumed uncertainty <0.5% of those from θ-S pairs [*Randall-Goodwin et al*., 2015]. Although the method of Jenkins [1999] has the advantage of coupling different pairs of tracers, it is difficult to define unequivocal water masses and a GMW end-member based on the extrapolation to zero-salinity [*Gade*, 1979]. Because the characteristics of each water mass can vary annually or seasonally, a massive hydrographic data set is also needed for each sampling period. A relatively larger discrepancy (∼0.4%) between the two approaches in St. 11 may be ascribed to this limitation. By contrast, the light noble gases, He and Ne, can be used to quantify the GMW fraction in seawater, especially when the hydrographic conditions are continually variable or only a limited data set is available. Nevertheless, both approaches still have some limitations for estimating the GMW in the surface layer because the "conservation of mass," an assumption adopted in both methods, is often invalid at the surface due to heat and gas exchanges with the overlying atmosphere.

3.5. Distribution of Excess He Along the Dotson Trough

Quantification of the GMW fraction using ΔHe and ΔNe is discussed in section 3.4. Here we investigated the ΔHe (and ΔNe) along the DT, which qualitatively reflect the GMW distributions in the deep water column of the Amundsen Sea. We note again that ΔHe (and ΔNe) cannot be used as quantitative tracers of GMW at the surface due to gas exchange. Because both ΔHe and ΔNe exhibited the same spatial distribution along the DT, we present only the ΔHe data in the figure for the sake of simplicity (Figure 6; refer to supporting information Figure S3 for ΔNe). We found that the large excess ΔHe (up to 14%) was present beyond the continental shelf break (St. 6), approximately 330 km from the DIS, especially at depths of 400–500 m. This large excess ΔHe suggests that the GMW is transported along the DT and directly influences seawater within hundreds of kilometers. This result is consistent with previous studies that reported a "melt-laden"

layer between 450 and 600 m at the northern extent of the DT [*Wåhlin et al.*, 2010; *Randall-Goodwin et al.*, 2015].

Along these stations (center of the DT), the layers between σ-$_\theta$ of 27.50 and 27.55 overlapped well with the maximum peak of ΔHe. Our LADCP observations suggest that the water at σ-$_\theta$ of 27.50 ($\sim$450 m depth) moves along the DT toward the continental shelf break (supporting information Figure S4). From the distribution of ΔHe along the DT and current directions of the maximum layer of ΔHe, we conclude that the majority of ΔHe in this region originated from the DIS and dispersed along the center of the DT (Figure 6) and that there was no significant water input crossing the ridge of the DT from adjacent troughs. Thus, the GMW plume from the DIS appears to be the most significant source of the excess ΔHe in the water column of the DT. Here we recognize that a fraction of this ΔHe may also originate from other melting ice shelves in the Amundsen Sea (e.g., some GMW input from Pine Island Bay) [*Nakayama et al.*, 2014]. Unfortunately, because of our limited observations in the center of the DT, we cannot assess either possible sources from outside the DT or the possibility that larger-scale ocean circulations influenced the GMW distributions in our study region. The ΔHe at the surface at Sts. 7 and 8 (sea-ice zone) is higher than that at Sts. 9 and 10 (the Amundsen Sea Polynya). This difference is attributed to the presence of sea ice at Sts. 7 and 8, which inhibits the gas exchange between the air and sea.

3.6. Distribution of Excess He Along Dotson and Getz Ice Shelves

We investigated the cross-sectional distributions of the ΔHe in front of the DIS and GIS in 2012. For most of the stations, the vertical distributions in the ΔHe of the DIS were similar to those of the GIS, which showed a subsurface maximum at $<$200 m depth (Figures 3 and 7). When fresh meltwater is initially formed near the grounding line depth, it does not immediately mix with the surrounding seawater. The fresh and buoyant meltwater gradually rises to the upper layer and entrains the surrounding water until it reaches a layer where it is no longer buoyant relative to the surrounding seawater [*Huppert and Josberger*, 1980]. Thus, the highest ΔHe (and GMW) can be found at a depth much shallower than that where GMW is initially formed. We note that the maximum ΔHe depth of $<$200 m in 2012 was much shallower than that in 2011 ($\sim$500 m).

The cross-sectional distributions of the ΔHe at the GIS were nearly uniform, indicating that the return flow of the mCDW, which includes the GMW, was not concentrated at a specific location (e.g., east versus west) or depth. These distributions were also observed in both θ and S in this region (Figure 7). Compared with the overall ΔHe distributions at the GIS, the ΔHe values were significantly higher at the DIS (Figures 3 and 7). This seems to be due to the local variations in the CDW input because the Coriolis force drags the CDW to the eastern slope of the DT and introduces larger portions of it to the DIS than the GIS. The ΔHe was highest ($<$200 m) in the westernmost part of the DIS (St. 27). Higher δ^3He and θ values were also observed at St. 27 (Figure 7). Our observations in 2012 agree with those of *Randall-Goodwin et al.* [2015] in 2011, indicating that a distinct outward flow occurs at the western side of the DT, with higher θ and S values and more GMW.

3.7. Temporal Variation of Excess He Along Dotson and Getz ice Shelves

Because we revisited the same stations for the DIS (St. 10 in 2011 and St. 19 in 2012) and GIS (St. 11 in 2011 and St. 24 in 2012), we can compare the temporal differences in the ΔHe and ΔNe in front of each ice shelf. We observed that both the ΔHe and ΔNe of the GIS and DIS were significantly lower in 2012 than those in 2011 (Figure 3 and supporting information Figure S2). It is likely that the decreases in ΔHe and ΔNe from 2011 to 2012 were related to the deepening of the top of the mCDW layers (from 400 to 650 m and from 650 to 750 m at DIS and GIS, respectively); that is, meltwater fractions at middepths appeared smaller when the thicknesses of mCDW were smaller in 2012. This is also consistent with the observation that the θ values of the CDW at the bottom of the DT region in 2011 ($\theta >1$°C) were higher than those in 2012 ($\theta \approx$ 0.6–0.8°C, supporting information Figure S5), indicating a weakening of the CDW intrusion to the DT region in 2012.

The decreases in the ΔHe and ΔNe observed at the GIS and DIS are consistent with the decreased glacial melting observed at the PIIS. *Dutrieux et al.* [2014] reported that the ice shelf melting of the PIIS decreased by 53% between January 2010 and 2012 probably due to a strong La Niña event. The melt rate of PIIS in 2012 was the lowest of five measurements during the past two decade. A similar reduction of the GMW at the PIIS and DIS, $>$300 km apart, may indicate that the basal melting rate in much of the Amundsen Sea is

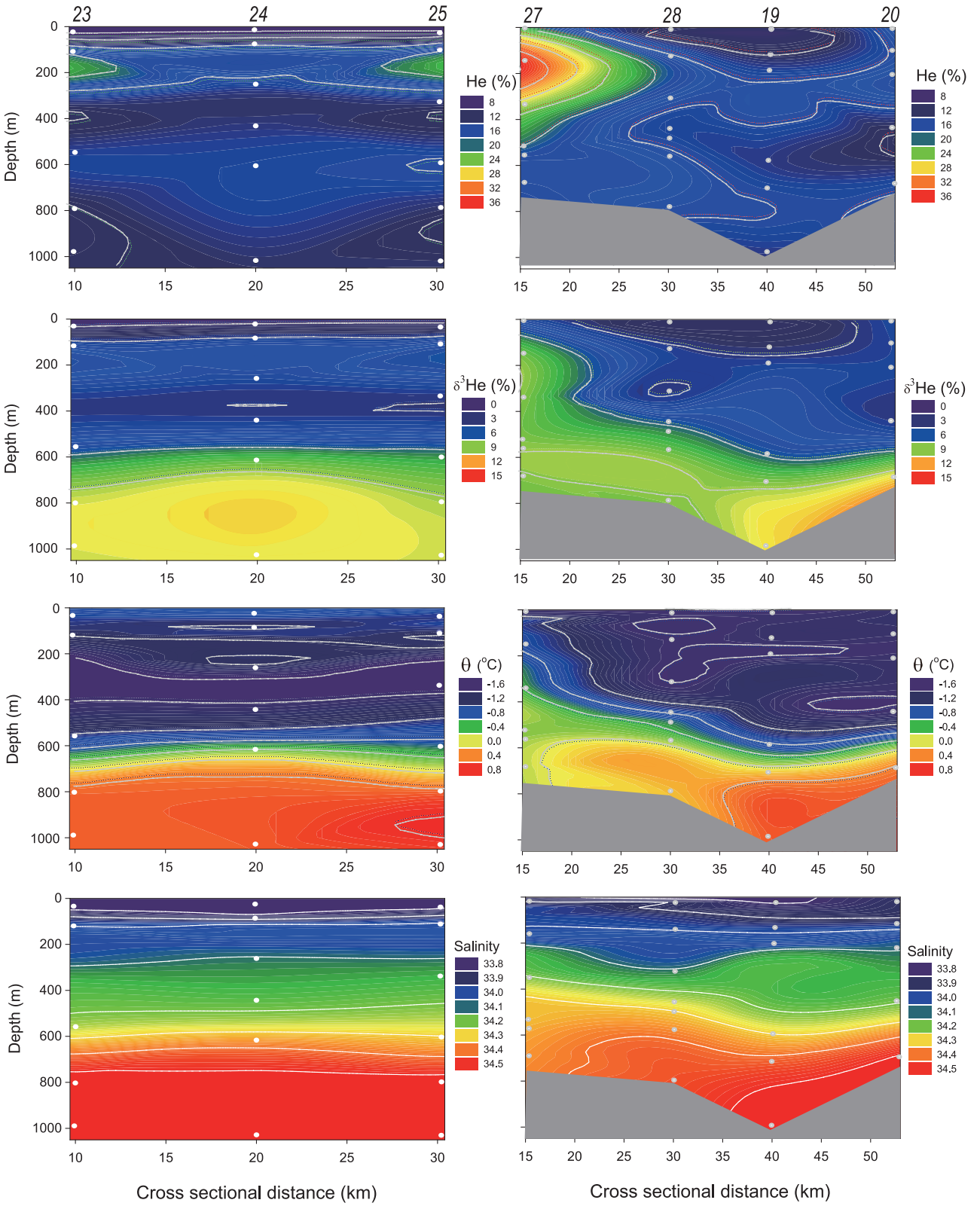

Figure 7. Distributions of ΔHe, δ^3He, θ, and S along the (left) GIS and (right) DIS in 2012. The station numbers are shown at the top of the figures. The black dots indicate the sampling depth for He (and Ne).

directly influenced by temporal variations of the CDW intrusion, likely driven by atmospheric forcing [*Dutrieux et al*., 2014].

Ha et al. [2014] observed that short-term variability (i.e., monthly changes) of temperature and current velocity was significant in the bottom layers of the DT. Thus, the highly variable bottom water intrusion is likely to result in substantial variations of the GMW in space and time. Although it is expected that studies with a higher temporal resolution will appear in the future, most of the satellite-based glacier melting studies were conducted over periods from several years to decades [*Pritchard et al*., 2012; *Rignot et al*., 2013]. Therefore, we note that shipboard meltwater observations including noble gases have advantages not only to capture short-term variability of basal melting rate but also to offer insights into meltwater pathways in water columns. Observations of water column properties including θ, S, noble gases, and oxygen isotopes will enhance the understanding of GMW variations over short temporal and spatial scales.

4. Conclusions

We investigated the spatiotemporal variations of the GMW by using the light noble gases He and Ne. The excess ΔHe (and ΔNe) was highest at depths of 400–500 m, the layer between the incoming CDW and the overlying WW along the entire center of the DT, and the large excess of ΔHe (and ΔNe) even extended outside of the shelf break (over 300 km from the ice shelves). These results indicate that the GMW from basal melting of the DIS and GIS is eventually transported several hundred kilometers offshore because the excess ΔHe (and ΔNe) mainly originated from glacial melting. Along the ice shelves, the highest ΔHe was observed in the western part of the DIS, indicating significant meltwater outflow. The ΔHe (and ΔNe) in 2012 decreased by up to 30–40% compared with 2011 at both ice shelves, suggesting a strong temporal variability of glacial melting. Using the excess ΔHe and ΔNe, we successfully quantified the GMW concentration in seawater, and the calculated GMW fraction in the Amundsen Sea water was in the range of 0.3–2.0%, which is similar to the range reported by *Randall-Goodwin et al*. [2015]. These results suggest that ΔHe and ΔNe are sensitive GMW tracers with high resolutions ($<$0.1% sensitivity). A recent study [*Loose and Jenkins*, 2014] has reported that the saturation anomaly ratios of heavy noble gases (Ar, Kr, and Xe) can be used to distinguish glacial melting from other physical processes that modify gas concentrations, such as seasonal changes in temperature at the ocean surface and bubble-mediated gas exchange. Thus, together with He and Ne studies, the coupling of heavy noble gas measurements (Ar, Kr, and Xe) can provide a robust method for tracing GMW. To more accurately investigate the distributions of GMW in the polar oceans, further in-depth discussions on quantifying the gas exchange loss of these tracers will be needed in the future.

Acknowledgments
We thank the captain and all the crew members of Araon, who helped with sampling on board. This work was supported by grant from Korea Polar Research Institute (PP15020). The data for this paper are available at Korea Polar Data Center (http://kpdc.kopri.re.kr).

References

Benson, B. B., and D. Krause Jr. (1980), Isotopic fractionation of helium during solution: A probe for the liquid state, *J. Solution Chem.*, *9*(12), 895–909.

Clarke, W. B., W. Jenkins, and Z. Top (1976), Determination of tritium by mass spectrometric measurement of ^{3}He, *Int. J. Appl. Radiat. Isotopes*, *27*(9), 515–522.

Depoorter, M., J. Bamber, J. Griggs, J. Lenaerts, S. Ligtenberg, M. van den Broeke, and G. Moholdt (2013), Calving fluxes and basal melt rates of Antarctic ice shelves, *Nature*, *502*(7469), 89–92.

Dutrieux, P., J. De Rydt, A. Jenkins, P. R. Holland, H. K. Ha, S. H. Lee, E. J. Steig, Q. Ding, E. P. Abrahamsen, and M. Schröder (2014), Strong sensitivity of Pine Island ice-shelf melting to climatic variability, *Science*, *343*(6167), 174–178.

Gade, H. G. (1979), Melting of ice in sea water: A primitive model with application to the Antarctic ice shelf and icebergs, *J. Phys. Oceanogr.*, *9*(1), 189–198.

Ha, H., A. Wåhlin, T. Kim, S. Lee, J. Lee, H. Lee, C. Hong, L. Arneborg, G. Björk, and O. Kalén (2014), Circulation and modification of warm deep water on the central Amundsen Shelf, *J. Phys. Oceanogr.*, *44*(5), 1493–1501.

Hahm, D., C. F. Postlethwaite, K. Tamaki, and K. R. Kim (2004), Mechanisms controlling the distribution of helium and neon in the Arctic seas: The case of the Knipovich Ridge, *Earth Planet. Sci. Lett.*, *229* (1), 125–139.

Hohmann, R., P. Schlosser, S. Jacobs, A. Ludin, and R. Weppernig (2002), Excess helium and neon in the southeast Pacific: Tracers for glacial meltwater, *J. Geophys. Res.*, *107*(C11), 3198, doi:10.1029/2000JC000378.

Hohmann, R., P. Schlosser, and B. Huber (2003), Helium 3 and dissolved oxygen balances in the upper waters of the Weddell Sea: Implications for oceanic heat fluxes, *J. Geophys. Res.*, *108*(C3), 3087, doi:10.1029/2000JC000474.

Huppert, H. E., and E. G. Josberger (1980), The melting of ice in cold stratified water, *J. Phys. Oceanogr.*, *10*(6), 953–960.

Jacobs, S., C. Giulivi, and P. Mele (2002), Freshening of the Ross Sea during the late 20th century, *Science*, *297*(5580), 386–389.

Jacobs, S., C. Giulivi, P. Dutrieux, E. Rignot, F. Nitsche, and J. Mouginot (2013), Getz IceShelf melting response to changes in ocean forcing, *J. Geophys. Res. Oceans*, *118*, 4152–4168, doi:10.1002/jgrc.20298.

Jacobs, S. S., and C. F. Giulivi (2010), Large multidecadal salinity trends near the Pacific-Antarctic continental margin, *J. Clim.*, *23*(17), 4508–4524.

Jacobs, S. S., A. Jenkins, C. F. Giulivi, and P. Dutrieux (2011), Stronger ocean circulation and increased melting under Pine Island Glacier ice shelf, *Nat. Geosci.*, *4*(8), 519–523.
Jenkins, A. (1999), The impact of melting ice on ocean waters, *J. Phys. Oceanogr.*, *29*(9), 2370–2381.
Jenkins, A., and S. Jacobs (2008), Circulation and melting beneath George VI ice shelf, Antarctica, *J. Geophys. Res.*, *113*, C04013, doi:10.1029/2007JC004449.
Jenkins, W. J., D. E. Lott, M. Davis, S. P. Birdwhistell, and M. O. Matthewson (1991), Measuring helium isotopes and tritium in seawater samples, *WOCE Hydrographic Operations and Methods*, WOCE Operations Manual, Vol. 3, Sec. 3.1, Part 3.1.3, WOCE Report No. 68/91, WHP Office WHPO 91-1.
Labasque, T., C. Chaumery, A. Aminot, and G. Kergoat (2004), Spectrophotometric Winkler determination of dissolved oxygen: Re-examination of critical factors and reliability, *Mar. Chem.*, *88*(1-2), 53–60, doi:10.1016/j.marchem.2004.03.004.
Loose, B., and W. J. Jenkins (2014), The five stable noble gases are sensitive unambiguous tracers of glacial meltwater, *Geophys. Res. Lett.*, *41*, 2835–2841, doi:10.1002/2013GL058804.
Martinerie, P., D. Raynaud, D. M. Etheridge, J.-M. Barnola, and D. Mazaudier (1992), Physical and climatic parameters which influence the air content in polar ice, *Earth Planet. Sci. Lett.*, *112*(1), 1–13.
Nakayama, Y., R. Timmermann, C. B. Rodehacke, M. Schroder, and H. H. Hellmer (2014), Modeling the spreading of glacial meltwater from the Amundsen and Bellingshausen Seas, *Geophys. Res. Lett.*, *41*, 7942–7949, doi:10.1002/2014GL061600.
Ozima, M., and F. A. Podosek (1983), *Noble Gas Geochemistry*, 367 pp., Cambridge Univ. Press, N. Y.
Padman, L., H. A. Fricker, R. Coleman, S. Howard, and L. Erofeeva (2002), A new tide model for the Antarctic ice shelves and seas, *Ann. Glaciol.*, *34*(1), 247–254.
Postlethwaite, C. (2002), Developing a tool for evaluating role of seasoanl sea ice in deep-water formation, PhD Thesis, University of Southampton, U. K.
Pritchard, H., S. Ligtenberg, H. Fricker, D. Vaughan, M. Van den Broeke, and L. Padman (2012), Antarctic ice-sheet loss driven by basal melting of ice shelves, *Nature*, *484*(7395), 502–505.
Randall-Goodwin, E., et al. (2015), Freshwater distributions and water mass structure in the Amundsen Sea Polynya region, Antarctica, *Elementa Sci. Anthropocene*, *3*(1), 000065.
Rignot, E., S. Jacobs, J. Mouginot, and B. Scheuchl (2013), Ice-shelf melting around Antarctica, *Science*, *341*(6143), 266–270.
Schlosser, P. (1986), Helium: A new tracer in Antarctic oceanography, *Nature*, *321*, 233–235.
Stanley, R. H., W. J. Jenkins, D. E. Lott, and S. C. Doney (2009), Noble gas constraints on air-sea gas exchange and bubble fluxes, *J. Geophys. Res.*, *114*, C11020, doi:10.1029/2009JC005396.
Thurnherr, A., S. Jacobs, P. Dutrieux, and C. Giulivi (2014), Export and circulation of ice cavity water in Pine Island Bay, West Antarctica, *J. Geophys. Res. Oceans*, *119*, 1754–1764, doi:10.1002/2013JC009307.
Thurnherr, A. M. (2010), A practical assessment of the errors associated with full-depth LADCP profiles obtained using Teledyne RDI Workhorse acoustic Doppler current profilers, *J. Atmos. Oceanic Technol.*, *27*(7), 1215–1227.
Wåhlin, A., X. Yuan, G. Björk, and C. Nohr (2010), Inflow of warm circumpolar deep water in the central Amundsen Shelf, *J. Phys. Oceanogr.*, *40*(6), 1427–1434.
Weiss, R. F. (1971), Solubility of helium and neon in water and seawater, *J. Chem. Eng. Data*, *16*(2), 235–241.
Winckler, G., R. Newton, P. Schlosser, and T. J. Crone (2010), Mantle helium reveals Southern Ocean hydrothermal venting, *Geophys. Res. Lett.*, *37*, L05601, doi:10.1029/2009GL042093.
Young, C., and J. Lupton (1983), An ultratight fluid sampling system using cold-welded copper tubing, *Eos Trans. AGU*, *64*, 735.